CrossMark

RESEARCH PAPER

A study on the characteristics of FSW tool shapes based on CFD analysis

Su-Deok Kim[1] · Jin-Young Yoon[2] · Suck-Joo Na[1]

Abstract In this study, computational fluid dynamics (CFD) was used to analyze the effect of tool shapes in friction stir welding (FSW). In FSW, a tool moves and rotates simultaneously so the interface between the tool and workpiece is changed at every time step. Frictional heat occurs at this interface, and in order to apply this heat, the interface should be tracked. A new interface tracking algorithm, which is applicable to any tool shape, was introduced to track the interface. Furthermore, an average area concept was used to calculate the interface area in each interface cell. This algorithm was applied to three tool shapes: cylinder, screw, and tap shapes. To validate the model, friction stir spot welding (FSSW) was performed for the cylinder type, and FSW was performed for the tap type. Temperature and torque history were compared with the experimental results. With the suggested algorithm, the velocity and viscosity distributions near the tool and the flow pattern obtained using a particle tracking method were used to analyze the characteristics of the tool shapes.

Recommended for publication by Commission III - Resistance Welding, Solid State Welding, and Allied Joining Process

✉ Suck-Joo Na
  sjoona@kaist.ac.kr

[1] Department of Mechanical Engineering, KAIST, Daejeon, Republic of Korea

[2] Advanced Welding and Joining Research Group, KITECH, Incheon, Republic of Korea

1 Introduction

Since friction stir welding (FSW) was developed at The Welding Institute (TWI) in 1991 [1], a great deal of research on the FSW simulations has been conducted and many heat source models have been developed successfully. FSW heat sources have been defined as volumetric heat source and interface heat source depending on a boundary condition. During FSW, tool is rotating and moving simultaneously, so many researchers have applied these heat source models as various ways of heat input. Nandan et al. [2] used a stationary tool with heat sources by frictional and viscous dissipation as boundary conditions. Chao YJ et al. [3] developed a finite element-based three-dimensional model of FSW. They applied a constant heat amount to the interface, which was modified until the results were consistent with the available experimental data. Similarly, S.D. Ji et al. [4] applied a steady-state temperature to the tool surface as a boundary condition, and Aljoaba et al. [5] applied the heat flux as an interface heat source with a stationary tool. Schmidt et al. [6] expressed an analytical interface heat generation model, which has been taken in various FSW simulations. They used this model with various contact conditions, such as sticking, sliding, and partial sticking, and compared one another to examine the effect of tool probe heat generation. However, this analytical model is not appropriate to three-dimensional cell, which heat was input as volumetric dimension, and complex tool shapes, which are difficult to integrate their model over shoulder or tool as they did in their paper.

Chen et al. [7] and Kim et al. [8] assumed a sticking condition and considered only plastic deformation heat source with the transformed ratio of about 0.9.

To express FSW process and apply heat sources, a lot of researchers have developed various mesh systems.

M. Song et al. [9] modeled a three-dimensional heat transfer model of FSW using a moving coordinate. They used frictional heat inputs from shoulder/workpiece and pin/workpiece interfaces.

The model was validated with measured temperature data. However, velocity or other information was not studied due to the difficulty of moving mesh system because data point is changed during simulations. Paul A. Colegrove et al. [10] simulated a complex tool shape using mesh generation program GAMBIT. They assumed that heat was generated by viscous dissipation. Using mesh generation system, tool rotating was successfully modeled, but inlet and outlet boundary conditions were chosen to express moving velocity of the tool. Tartakovsky et al. [11] proposed a Lagrangian-based smoothed particle hydrodynamics (SPH) method. They applied heat sources at interface and by viscos dissipation. This method has several advantages for FSW simulations. Similarly, Schmidt et al. [12] used ALE method and they could predict void formation. But SPH and other Lagrangian method need higher computational costs than grid-based method. Recently, Kim et al. [13] applied both heat sources and expressed the rotating and moving motions by their geometric relation. They used a grid-based mesh system and expressed the tool motions well, but their method is only applicable to cylindrical tool shapes. Even though numerous FSW papers have been published, most of their works were based on many assumptions, which caused by difficulties to be expressed in a simulation.

The goal of this paper is to propose a new model with grid-based system to express the rotating and moving motions of a tool simultaneously, which has been assumed as boundary conditions in previous papers, and analyze velocity, viscosity distribution, and flow pattern of various tool shapes for the study of their characteristics.

2 Methodology

2.1 Viscosity modeling

Viscosity can be expressed as a function of temperature and strain rate, and for its calculation, the flow stress suggested by Sheppard et al. [14] is calculated by the following:

$$\sigma_e = \frac{1}{\alpha}\sinh^{-1}\left[\left(\frac{Z}{A}\right)^{\frac{1}{n}}\right]$$

where A, α, and n are material constant and Z is the Zener-Hollomon parameter given by the following:

$$Z = \dot{\bar{\varepsilon}}\exp\left(\frac{Q}{RT}\right)$$

where Q is the activation energy, R is a gas constant, T is the temperature, and $\dot{\bar{\varepsilon}}$ is the effective strain rate, which is given by the following:

$$\dot{\bar{\varepsilon}} = \left(\frac{2}{3}\varepsilon_{ij}\varepsilon_{ij}\right)^{\frac{1}{2}}$$

Table 1 Data used in the simulations

Properties	Value
Workpiece material	AA5052
Material constant, A	exp(24.47)
Material constant, α	0.016 MPa^{-1}
Material constant, n	5.24
Material constant, Q	155,167 J

where $\dot{\varepsilon}_{ij}$ is the strain rate tensor, given by the following:

$$\varepsilon_{ij} = \frac{1}{2}\left(\frac{\partial u_i}{\partial x_j} + \frac{\partial u_j}{\partial x_i}\right)$$

In Sheppard's paper [15], he found material constants of his equation for various materials. In this paper, AA5056 was used, and data are shown in Table 1.

Finally, Perzyna's visco-plasticity model [16] can be calculated from the above equations by the following:

$$\mu = \frac{\sigma_e}{3\dot{\bar{\varepsilon}}}$$

2.2 Interface tracking and heat generation

The open area concept was introduced to track the interface cells. In this concept, the three positive surfaces of a three-dimensional cell, $+x$, $+y$, and $+z$ surfaces, give the fraction of hidden area ratio by a tool when a tool meets cells. If the fraction is less than 1, which means that some parts of a cell are hidden by the tool, those cells are considered interface cells. This concept is illustrated in Fig. 1.

After tracking all the interface cells, the average area concept was used. Initially, a tool was divided into four sections, the shoulder side, shoulder tip, pin side, and pin tip, as shown in Fig. 2. The surface area of each section was calculated, and by dividing it by the number of interface cells of each section, the average area in an interface cell was calculated to apply interface heat. Let S is the area of shoulder side, which was initially calculated, and N is the interface cell in the shoulder side, which was counted during every time step, then S/N gives the average area of each cells in the shoulder side. This concept was also applied to the other sections, shoulder tip, pin side, and pin tip, to apply interface heat of each section. For the contact condition between the tool and workpiece, a slip condition was assumed, and this condition is expressed by the following:

$$\tau = mk$$

where τ is the shear stress, m is the fraction factor, and k is the maximum shear stress at yielding, which is given as dividing yield strength by $\sqrt{3}$ based on Von-Mises yield criteria. The friction factor, m, was chosen as 0.4. In a slip condition, the

Fig. 1 **a** The three positive surfaces of a three-dimensional cell. **b** Interface cell tracking example (+z cell is activated and the fraction is less than 1)

Fig. 2 The four sections for initial area calculation (screw type)
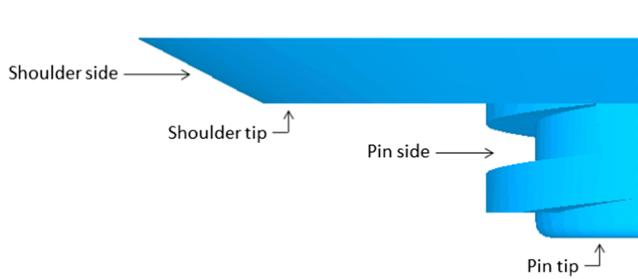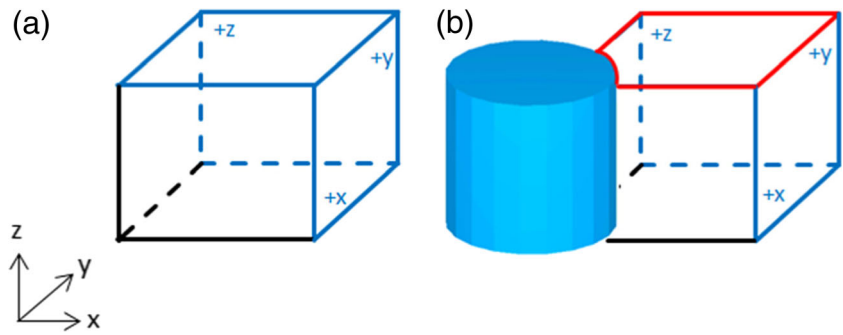
friction factor could be defined as a value from 0 to 1. In the paper by Buffa et al. [17], various friction factors were simulated and the value of 0.4 was followed well with experimental results. So the shear factor value of 0.4 was used in the simulation. With this condition, the interface heat was applied by the following:

$$q_i = \frac{mk\omega r A_r}{V}$$
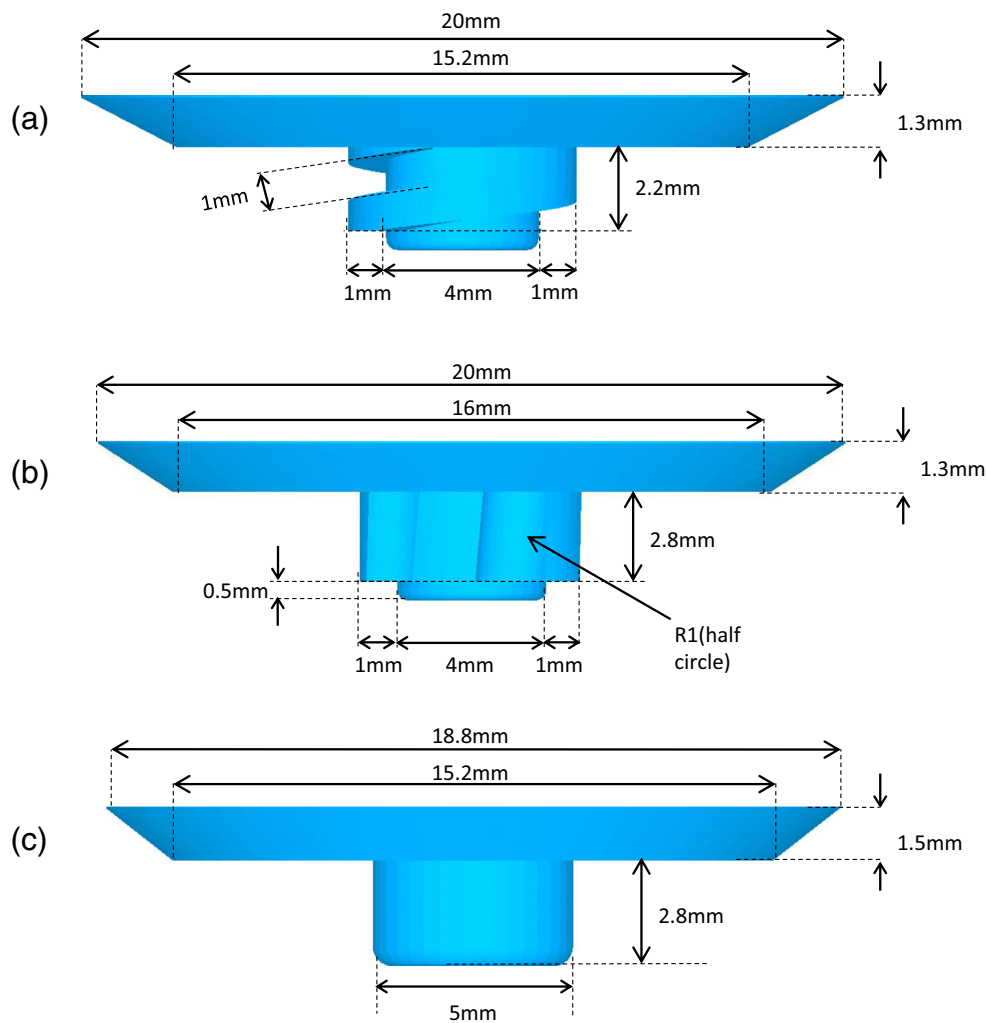
Fig. 3 Tool types used in the simulation: **a** cylinder type, **b** screw type, and **c** tap type

Table 2 Welding conditions

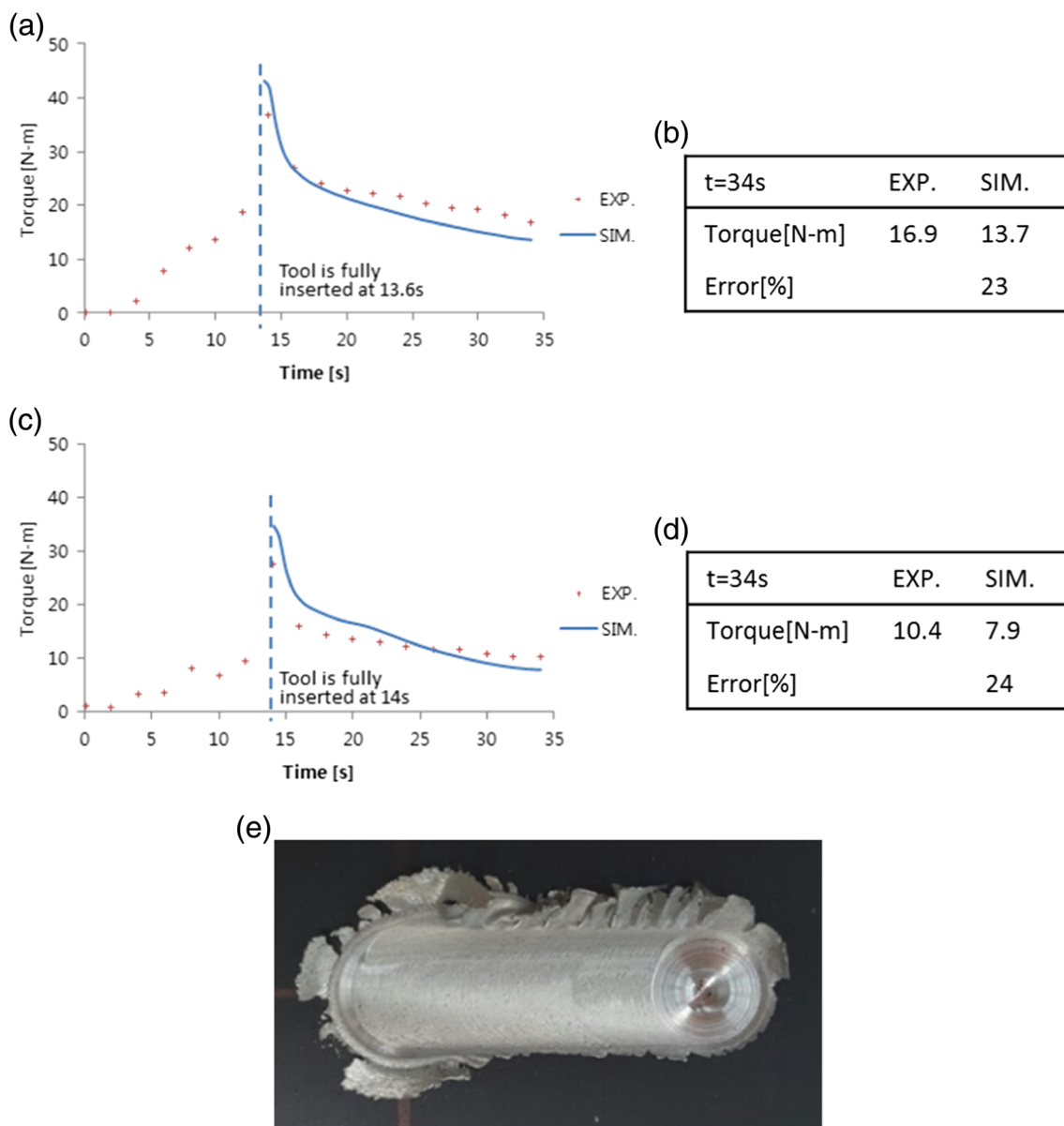| Property/weld parameter	FSW (cylinder, screw, tap)	FSSW (cylinder)
Workpiece length (mm)	100	60
Workpiece width (mm)	60	60
Workpiece depth (mm)	40	40
Weld speed (mm/min)	50	
Rotational speed (rpm)	600	1000

where q_i is the interface heat generation rate, ω is the rotational speed, r is the distance between the tool center and a interface cell, A_r is the interface area, and V is the cell volume enclosing

interface cell. Plastic deformation heat can be expressed by the following [18, 19]:

$$q_p = f_m \sigma_e \dot{\bar{\varepsilon}}$$

where q_p is the plastic deformation heat generation rate, f_m is the transformed ratio from plastic work to heat, and $\dot{\bar{\varepsilon}}$ is the effective strain rate. The transformed ratio value of 0.9 was used because in aluminum alloy, this ratio has been defined as 0.8 to 1 in previous research [7, 8, 20]. This value resulted in about 4~5% of volumetric heat amount of the total heat amount as Nandan's work [2].

Using user subroutines mainly QSADD and MUCAL subroutines, above models were applied. QSADD subroutine defines

(a)

(b)

t=34s	EXP.	SIM.
Torque[N-m]	16.9	13.7
Error[%]		23

(c)

(d)

t=34s	EXP.	SIM.
Torque[N-m]	10.4	7.9
Error[%]		24

(e)

Fig. 4 Torque comparison for FSW (**a**, **b**) and for FSSW (**c**, **d**), and burr effect for FSW (**e**)
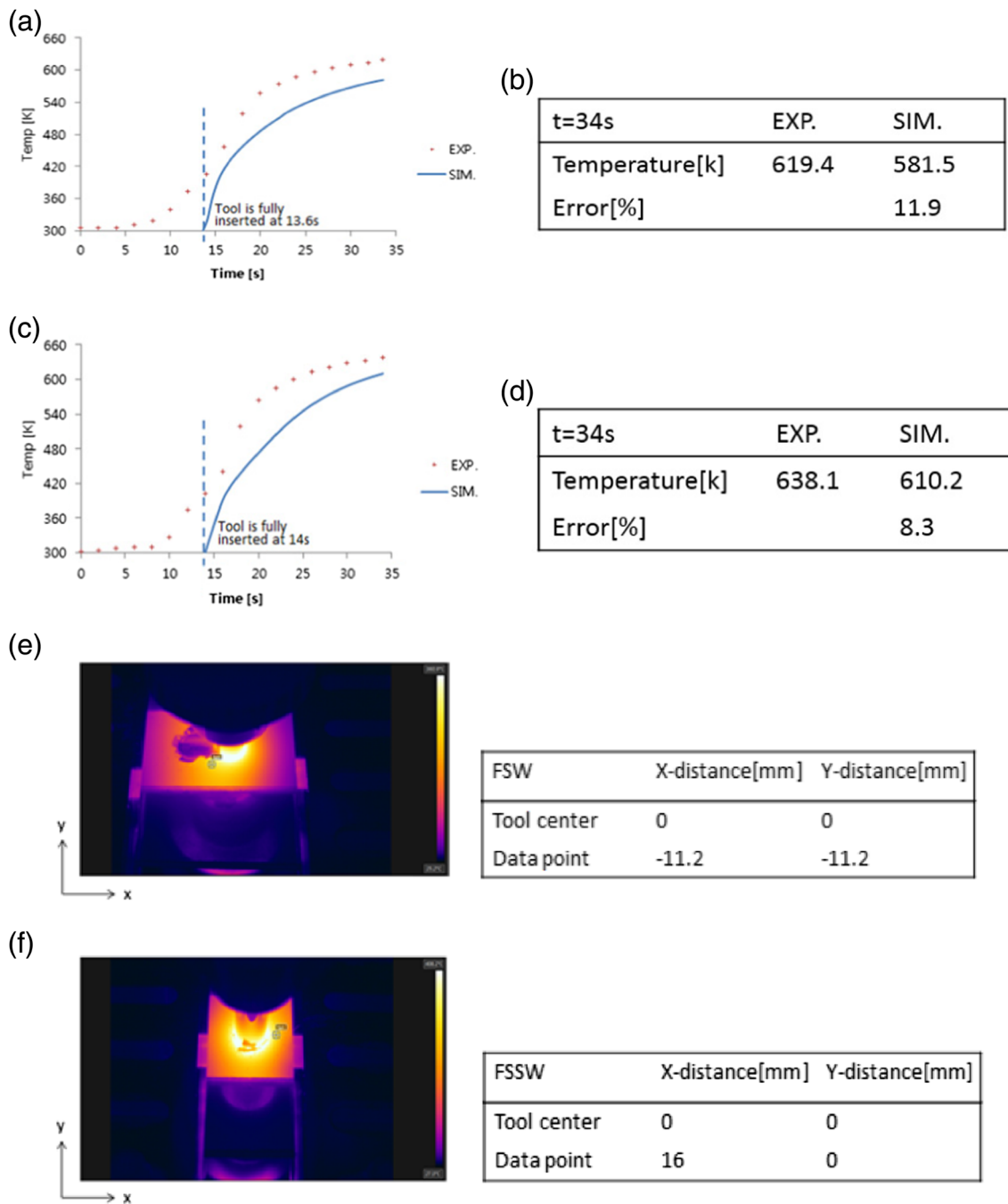
Fig. 5 Temperature comparison for FSW (**a, b**) and for FSSW (**c, d**), and locations for temperature measurement for FSW (**e**) and for FSSW (**f**)

specific energy in a cell, so the interface algorithm and heat generation models were implemented in this subroutine. MUCAL subroutine defines viscosity in a cell, and this subroutine works after heat is applied to a cell by QSADD subroutine. This procedure is repeated in every time step until simulation is finished.

2.3 Simulation conditions

Velocity boundary conditions between tool surface and workpiece were assumed to be sticking. This may conflict with the slip condition used, but heat generation by plastic deformation, which is related to velocity gradients, is about 5%, so this assumption would not much affect the total heat generation. Because velocity boundary conditions define velocity magnitude of interface cells, for velocity, viscosity, and flow pattern analysis, this assumption is reasonable. Figure 3 shows the three types of tool used in the simulations. For validation of the suggested algorithm, friction stir spot welding (FSSW) and FSW were performed. FSSW was performed with the cylinder type, and FSW was performed with the cylinder,

screw, and tap types. The experiment was also performed with the same conditions. The simulation conditions are shown in Table 2.

## 3 Results and discussion

3.1 Model validation

Mesh tests were conducted with the size of 0.4 and 0.6 mm for ensuring that velocity and viscosity fields are accurate in the mesh size used. Both the size of 0.4 and 0.6 mm yielded a similar trend, and velocity and viscosity values in each cells were almost the same. But in this paper, the mesh size of 0.4 mm was used because this value gave more accurate heat generation in preliminary simulations. Mesh sizes smaller than 0.4 mm were not tested because the computation costs increase rapidly. As discussed, the tool is initially inserted into the workpiece, and thus, the plunging phase is not considered. The simulation results were compared with the experimental results after the tool was fully inserted into the workpiece, i.e., after 13.6 s for FSW and 14 s for FSSW, as shown in Fig. 4a, c, respectively. Simulations were performed until the temporal rate of change of temperature and torque was less than 3%. Figure 4 shows the torque comparison of FSW and FSSW, respectively. The simulated results follow a similar trend with

the experimental results, but in both cases, the simulated results are about 25% (around 3[N-m]) less than the experimental values at 34 s, where the simulation was finished. Figure 5 shows the temperature comparison of FSW and FSSW, respectively. The locations for temperature measurement were roughly 16 mm away from the tool center, and the data point was moving with the same speed with that of the tool during the FSW process. The simulated temperature profiles also have a similar trend but around 12% difference (around 30 K) at 34 s is observed. From the simulation results, the calculated temperature and torque have lower values than those from the experimental results. This is ascribed to the small workpiece, which moves up along the tool shoulder while the tool is inserted, as shown in Fig. 4e, during the experiments. The tool consequently requires additional torque and generates an increased amount of heat during the process, which was not considered in the simulation. Thus, both temperature and torque from the experiment have increased values relative to the calculated results. The torque measurement device was attached directly to the tool, and this additional torque has a relatively huge effect on the measured torque, resulting in a 25% difference. Temperature was measured at points away from the moved workpiece as shown in Fig. 5e, f to reduce the effect of this increased amount of heat on the measured temperature, which led to approximately a 12% difference. Even though there is a little difference
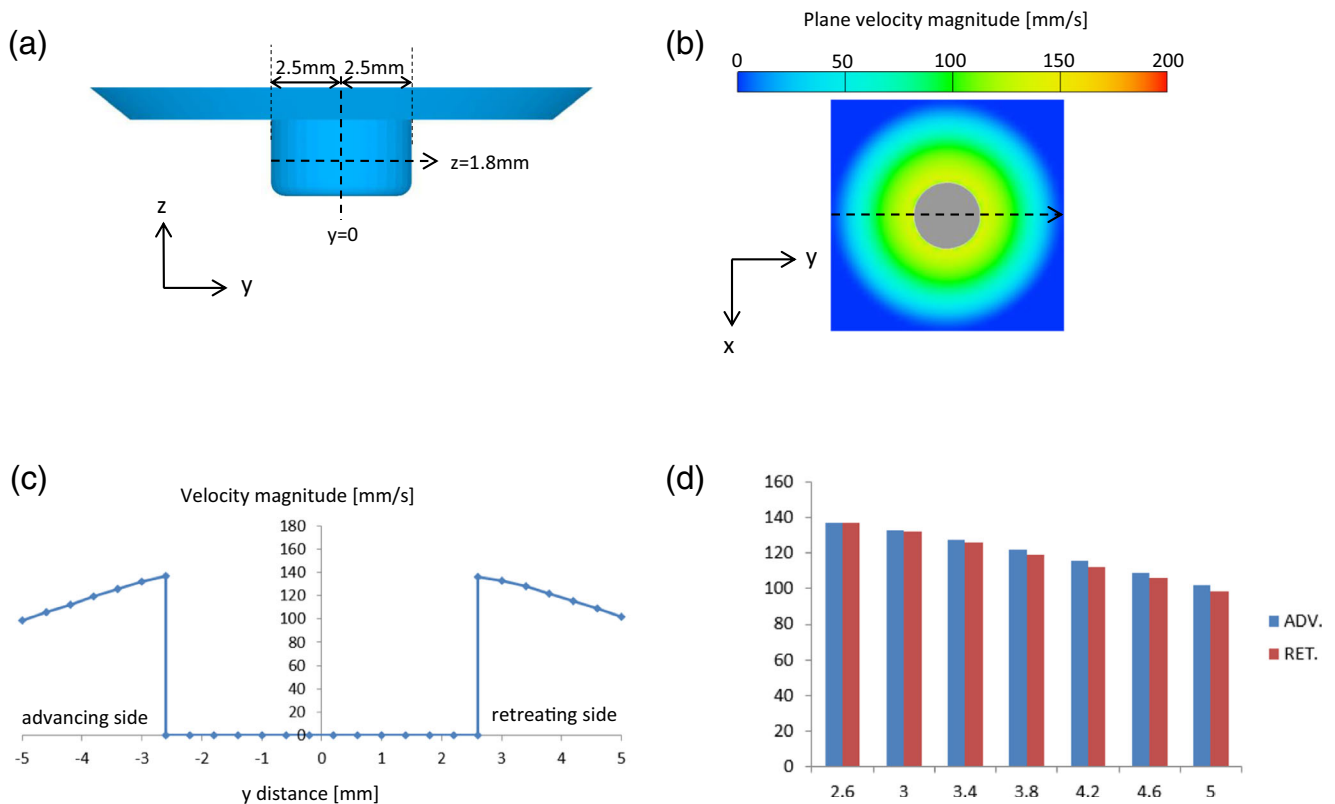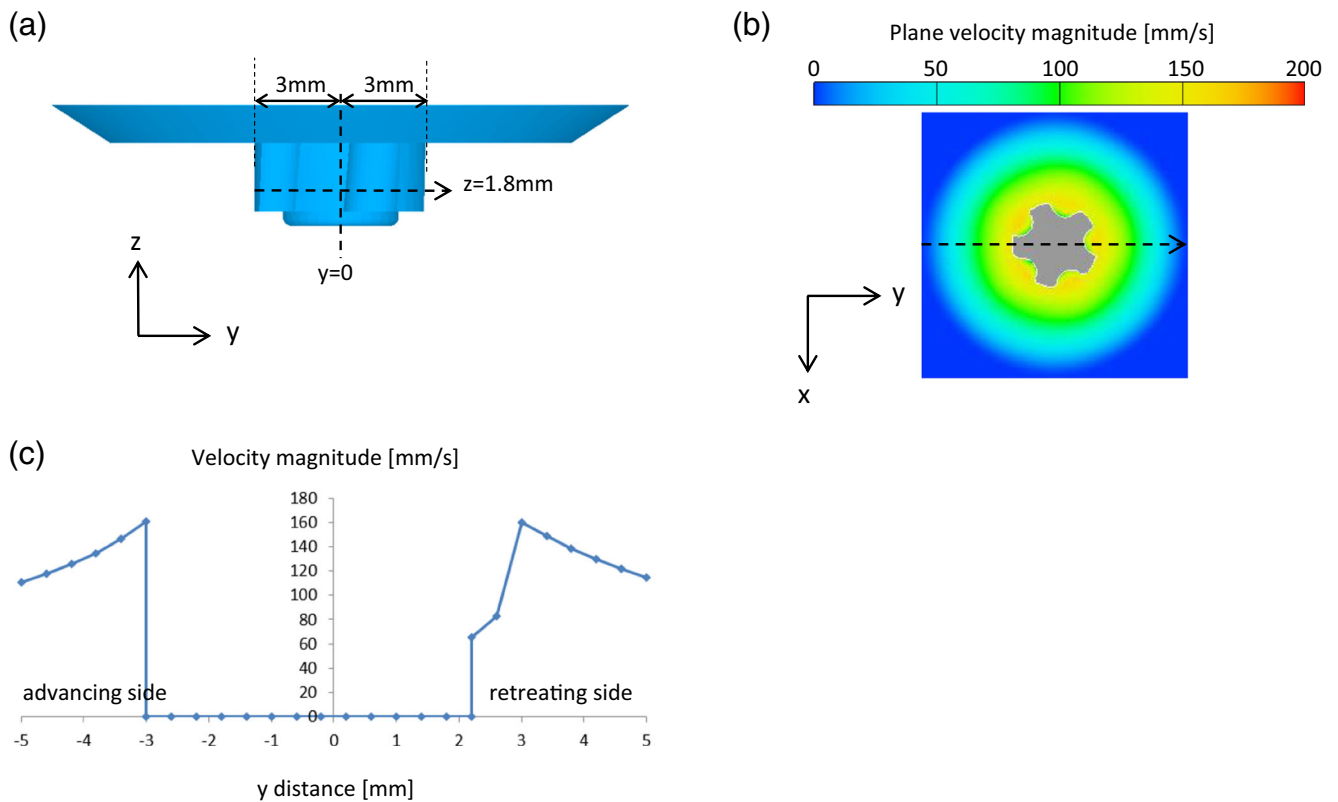

Fig. 6 Velocity magnitude of cylinder type; **a** *YZ* plane geometry, **b** *XY* plane velocity magnitude, **c** velocity magnitude along *y* distance, and **d** velocity magnitude comparison between advancing side and retreating side
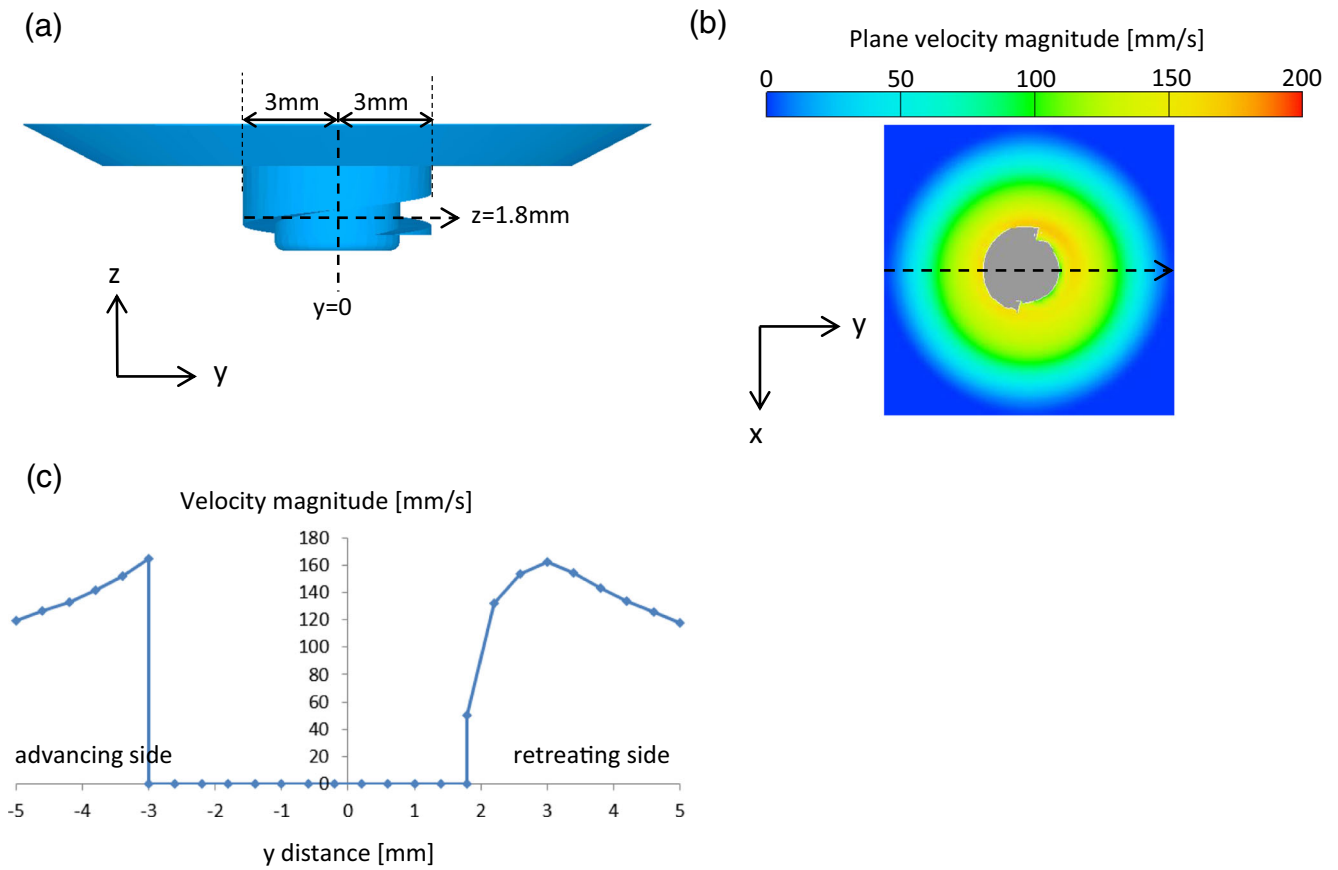
Fig. 7 Velocity magnitude of screw type; **a** *YZ* plane, **b** *XY* plane velocity magnitude, and **c** velocity magnitude along *y* distance


Fig. 8 Velocity magnitude of tap type; **a** *YZ* plane geometry, **b** *XY* plane velocity magnitude, and **c** velocity magnitude along *y* distance

between the experimental and calculated results, a similar trend is observed, and thus, the suggested model can be used to predict torque and temperature profiles.

3.2 Velocity distribution

The velocity magnitude was calculated along the y-direction at $z = 18$ mm. The cylindrical tool shape has a symmetric pin geometry, and hence, the velocity distribution near the pin is also symmetric as shown in Fig. 6b, c. The velocity magnitude has a maximum value at the pin surface and gradually decreases moving away from the pin surface. Also, the velocity magnitude at the advancing side is bigger than that at the retreating side, and this difference increases moving from

the pin surface as shown in Fig. 6d. This is because the velocity vectors by tool rotating and moving have the same direction at the advancing side and the opposite at the retreating side. For the screw type, the velocity at the advancing side starts to develop at 3 mm, which is the outer pin radius, as shown in Fig. 7a, and then decreases moving away from the surface, as shown in Fig. 7c. The velocity at the retreating side starts to develop at 1.8 mm, which is the inner pin radius, and reaches the maximum at 3 mm. For the tap type, the velocity distribution is also asymmetric due to the pin geometry, and the velocity has a maximum value at 3 mm, which is the outer pin radius, as shown in Fig. 8a–c. Like the screw type results, the velocity magnitude near the inner surface is not the maximum at the pin surface, and increases and reaches the
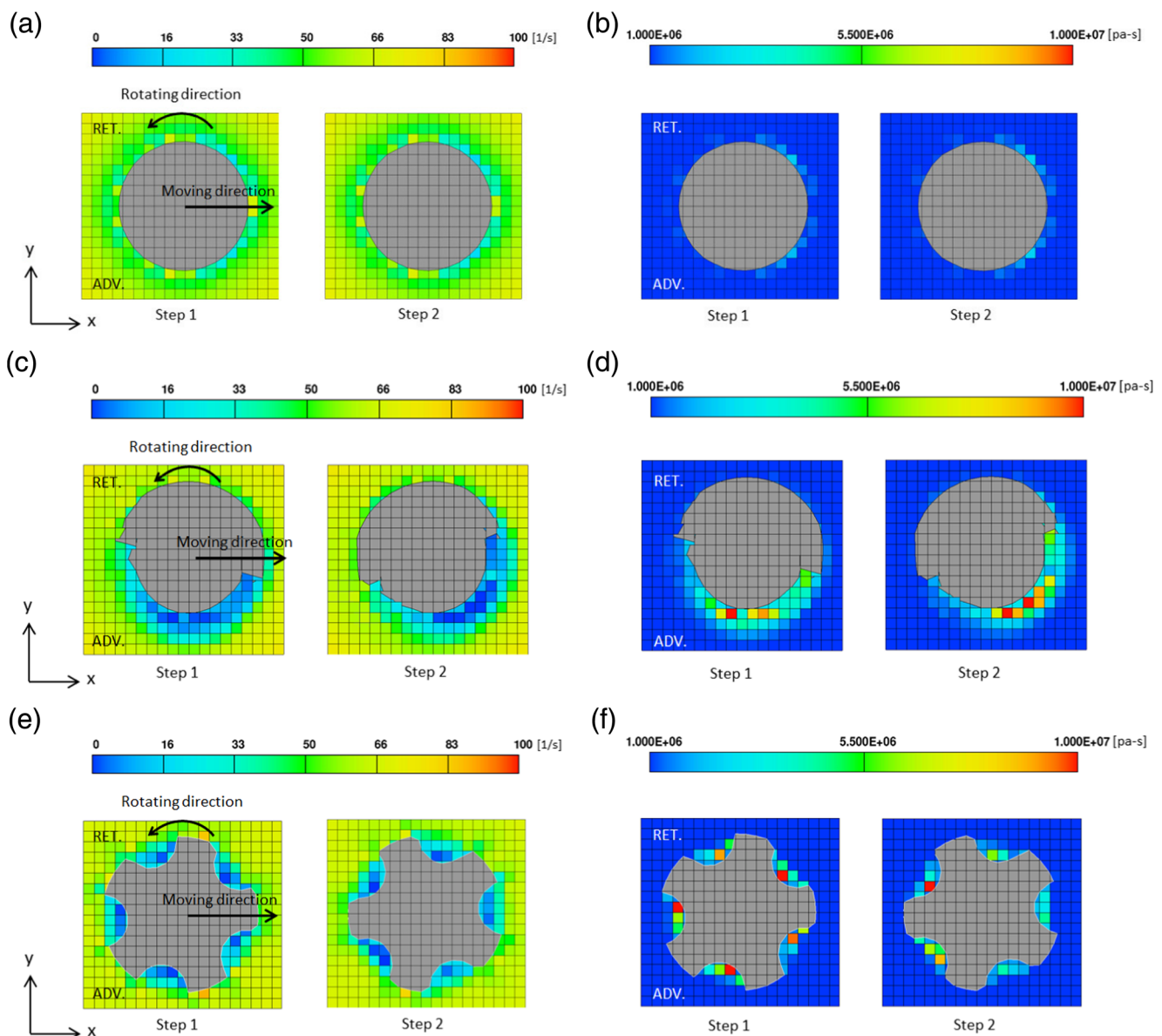
Fig. 9 Effective strain rate distribution near the tool at $z = 1.8$ mm; cylinder (a), screw (c), and tap (e) types. Viscosity distribution near the tool at $z = 1.8$ mm; cylinder (b), screw (d), and tap (f) types.

maximum at the outer pin radius. This is because the velocity generated by the adjacent outer pin surface affects the velocity at the inner pin surface. Thus, it is thought that different pin radii of a pin will affect the velocity distribution near the surface, which will affect the viscosity distribution.

3.3 Viscosity distribution

The viscosity and the effective strain rate near the pin were calculated on the XY plane at $z = 18$ mm, as shown Fig. 9. In all the cases, the zones with lower effective strain rate yield a higher viscosity than other zones. In the cylinder case, the viscosity around the pin at the front side, which the tool moves to, is higher than that at the back side. The tool surface at the front side is moving through the workpiece during the welding process, and thus, the velocity near this zone is not well distributed, which causes a smaller effective strain rate and a higher viscosity than the values at the back side. Also, the viscosity distribution at the advancing side and the retreating side is nearly the same. In the screw case, the viscosity near the inner pin surface is higher than that at the outer pin surface. As discussed in the velocity analysis, the velocity near the inner pin surface is smaller than that in other zones, and

consequently, a less effective strain rate and a higher viscosity are obtained. The viscosity distribution becomes uniform moving from this zone. Except for this zone, there is not much difference between the advancing side and the retreating side. The tap type tool has five inner zones, and every zone yields a smaller effective strain rate and a higher viscosity than other zones, as shown in Fig. 9e, f, corresponding with the phenomena observed form the screw type results. Also, the viscosity distribution at the advancing side and the retreating side is nearly the same except for at the five inner zones. Thus, it is assumed that the zones with radial differences in a pin will have a severe velocity gradient and thereby cause non-uniform distributions of velocity, effective strain rate, and viscosity, which will affect the welding quality.

3.4 Flow pattern

In order to analyze the fluid flow during the welding process, massless particles were applied. Figure 10a shows the initial particle positions for the screw type, and Fig. 10b–f shows the change of the radial distance of each particle at 0 to 1, 50 to 51, and 100 to 101 revolutions, respectively. In all the cases, the radial
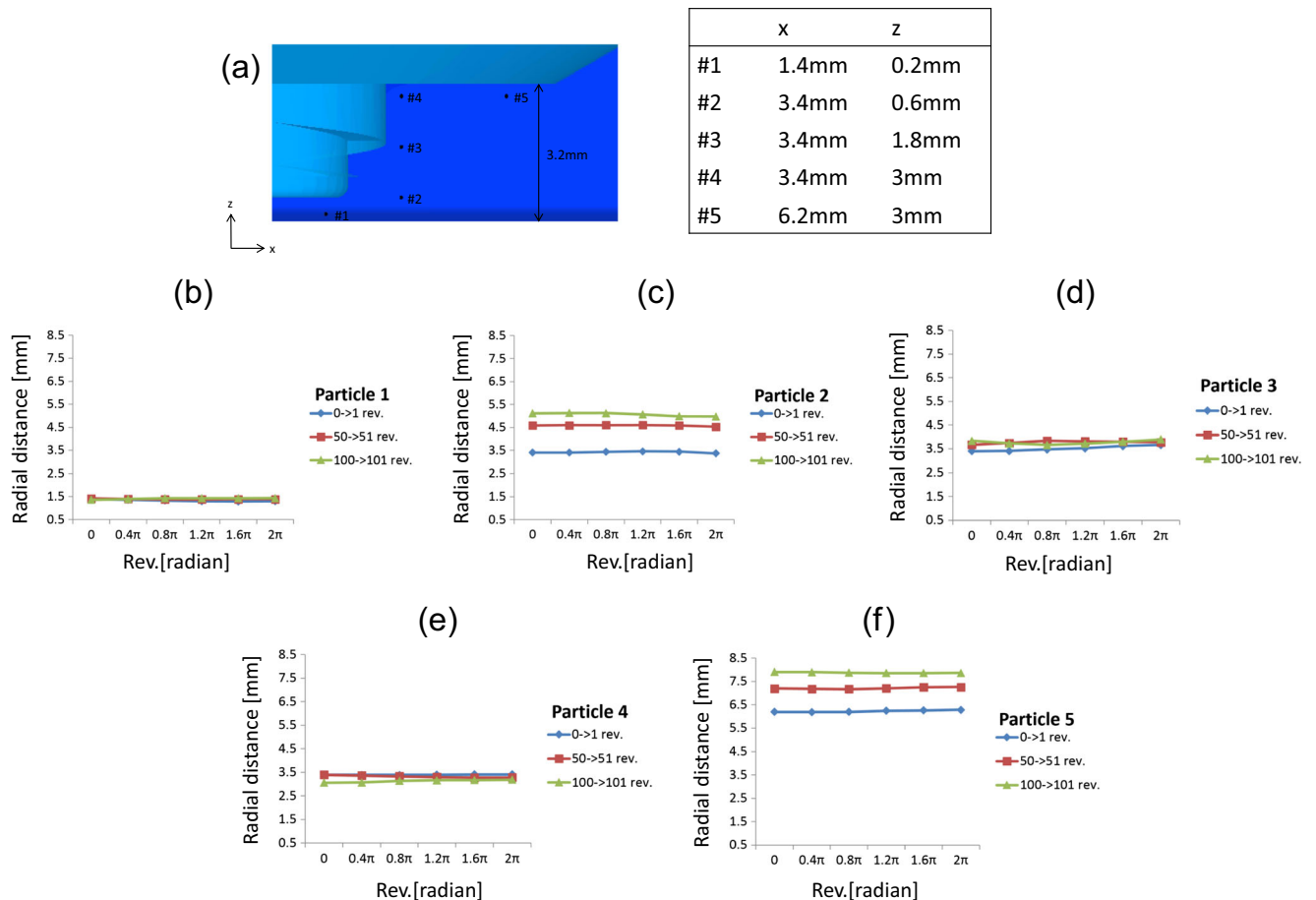
	x	z
#1	1.4mm	0.2mm
#2	3.4mm	0.6mm
#3	3.4mm	1.8mm
#4	3.4mm	3mm
#5	6.2mm	3mm

Fig. 10 Particle tracing for screw type: **a** initial particle coordinates and **b–f** particle position
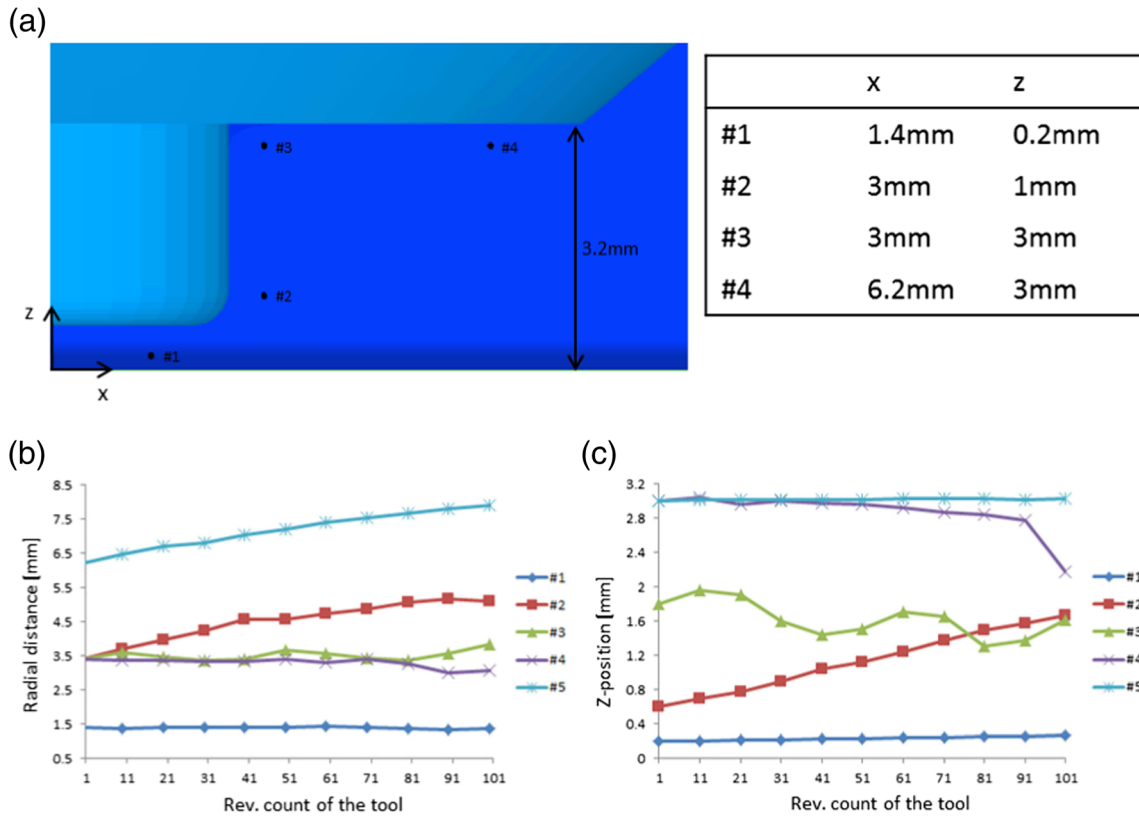
Fig. 11 Particle tracing for cylinder type: **a** initial particle coordinates, **b** radial distance, and **c** z-position
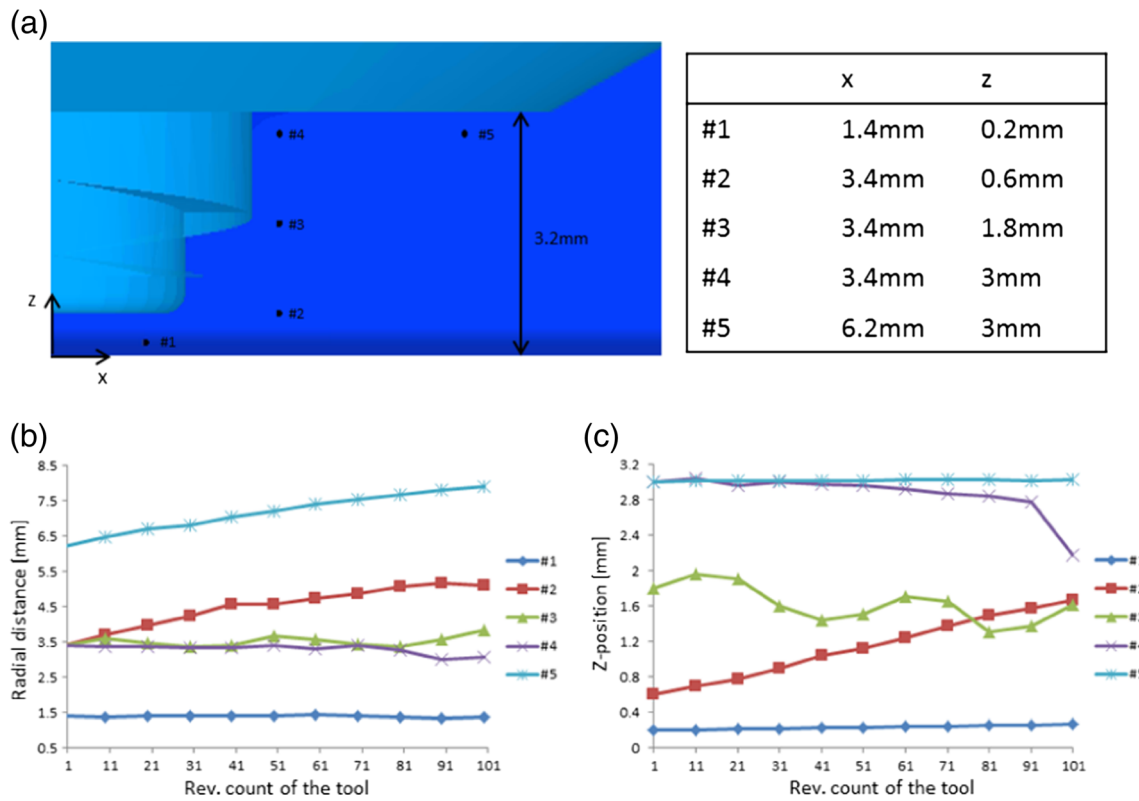

Fig. 12 Particle tracing for screw type: **a** initial particle coordinates, **b** radial distance, and **c** z-position
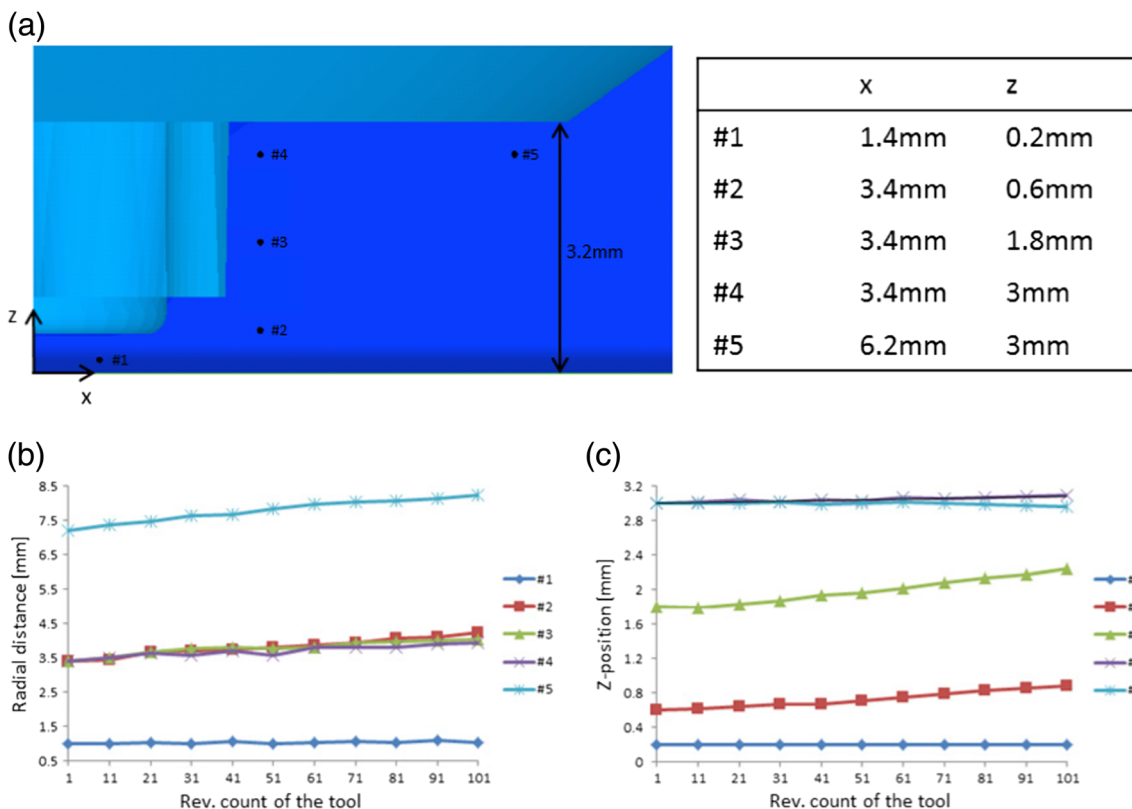
(a)

	x	z
#1	1.4mm	0.2mm
#2	3.4mm	0.6mm
#3	3.4mm	1.8mm
#4	3.4mm	3mm
#5	6.2mm	3mm

(b)

(c)

Fig. 13 Particle tracing for tap type: **a** initial particle coordinates, **b** radial distance, and **c** z-position

distance of each particle is not substantially changed at each revolution. However, some particles are changed as the revolutions are increased, such as particles 2 and 3, and this phenomenon is also observed in the cylinder and tap cases. Thus, the change of radial distance and z-position of each particle as revolutions are increased was studied.

In the cylinder case, particles 1 and 2 nearly maintain the initial distances. Particles 3 and 4 move away from the tool center, as shown in Fig. 11b. However, the z-position of all the particles is maintained at the initial value, as shown in Fig. 11c. Thus, as the tool rotates, fluid below the shoulder flows away from the center in the radial direction, and there is not much vertical flow in all positions in the cylinder type case.

In the screw type case, five particles were applied, and the initial position of each particle is shown in Fig. 12a. Particle 1 nearly maintains the initial radial distance and z-position. Particle 2 moves away from the tool center and moves to the shoulder. Particle 3 fluctuates in the radial and vertical directions. Particle 4 retains the initial radial distance and z-position until nearly the 80th revolution and then moves slightly to the tool center and to the bottom. Particle 5 moves away from the tool center and maintains the initial z-position. Thus, in the screw type, fluid flows away from the center in the radial direction and to the shoulder in the vertical direction near the pin tip. Also,

fluid fluctuates in both radial and vertical directions near the middle of the tool and flows to the center in the radial direction and to the bottom in the vertical direction after the 80th revolution near the pin top.

In the tap case, also five particles were applied, and the initial position of each particle is shown in Fig. 13a. Particle 1 nearly maintains the initial radial distance and z-position. Particles 2 and 3 move away from the center and to the shoulder. Particle 4 moves away from the center and slightly to the bottom. Particle 5 moves away from the center and nearly maintains the initial z-position. Thus, in the tap type, fluid near the pin flows away from the center in the radial direction and to the shoulder in the vertical direction except for the pin tip.

In all the cases, fluid below the pin tip has no radial or vertical flow, and fluid below the shoulder tip flows away from the center and nearly maintains the initial z-positions.

4 Conclusion

The results of this study are summarized as follows:

1. An interface tracking algorithm was introduced and applied to three different tool shapes.
2. FSW (for the tap type) and FSSW (for the cylinder type) were performed for validation.

- Temperature profiles follow a similar trend as the experimental results but have approximately a 12% difference.
- Torque profiles follow a similar trend as the experimental results but with roughly a 25% difference
- The difference was from the moved workpiece generated by the plunging phase.

3. The velocity distribution was studied.

- The cylinder type has an almost symmetric velocity distribution, and velocity at the advancing side was larger than that at the retreating side.
- The screw and tap types have an asymmetric velocity distribution, and different radii of the pin yield a velocity gradient.

4. Viscosity and effective strain rate distribution were studied.

- The cylinder type has higher viscosity at the front side and similar distributions at both the advancing and retreating side.
- The screw and tap types have a higher viscosity near the inner surface of the pin and similar distributions at both the advancing and retreating side except for the inner zones.

5. Flow pattern near the tool was studied

- The cylinder type tool creates a radial direction flow near the pin top but does not create vertical direction fluid.
- The screw type tool creates a complex flow and in particular a fluctuating flow near the middle of the pin.
- The tap type creates a flow away from the center and to the shoulder near the pin.
- In all the types, fluid below the pin tip does not create radial or vertical direction flow.

Reference

1. Thomas, W. M., et al 1991 The Welding Institute, TWI, *International Patent Application* No. 9125978.8. PCT/GB92/02203 and GB Patent Application

2. Nandan R et al (2007) Three-dimensional heat and material flow during friction stir welding of mild steel. Acta Mater 55(3):883–895

3. Chao YJ, Qi X (1998) Thermal and thermo-mechanical modeling of friction stir welding of aluminum alloy 6061-T6. J Mater Process Manuf Sci 7:215–233

4. Ji SD et al (2012) Numerical simulation of material flow behavior of friction stir welding influenced by rotational tool geometry. Comput Mater Sci 63:218–226

5. Aljoaba SZ et al (2009) Modeling of friction stir processing using 3D CFD analysis. Int J Mater Form 2:315–318

6. HNB Schmidt, J Hattel (2004) Heat source models in simulation of heat flow in friction stir welding. Int J Offshore Polar Eng 14(04)

7. Chen G-q et al (2013) Computational fluid dynamics studies on heat generation during friction stir welding of aluminum alloy. Comput Mater Sci 79:540–546

8. Kim D et al (2010) Numerical simulation of friction stir butt welding process for AA5083-H18 sheets. European Journal of Mechanics-A/Solids 29(2):204–215

9. Song M, Kovacevic R (2003) Thermal modeling of friction stir welding in a moving coordinate system and its validation. Int J Mach Tools Manuf 43(6):605–615

10. Colegrove PA, Shercliff HR (2005) 3-Dimensional CFD modelling of flow round a threaded friction stir welding tool profile. J Mater Process Technol 169(2):320–327

11. Tartakovsky, Alexandre, et al (2006) Modeling of friction stir welding (FSW) process with smooth particle hydrodynamics (SPH). No. 2006–01-1394. SAE Technical Paper

12. Schmidt H, Hattel J (2004) A local model for the thermomechanical conditions in friction stir welding. Model Simul Mater Sci Eng 13(1):77

13. Kim S-D, Na S-J (2016) A study on an interface tracking algorithm in friction stir welding based on computational fluid dynamics analysis. Journal of Welding and Joining 34(3):12–16

14. Sheppard T, Wright DS (1979) Determination of flow stress: part 1 constitutive equation for aluminum alloys at elevated temperatures. Metals Technology 6(1):215–223

15. Sheppard T, Jackson A (1997) Constitutive equations for use in prediction of flow stress during extrusion of aluminium alloys. Mater Sci Technol 13(3):203–209

16. Zienkiewicz OC, Cormeau IC (1974) Visco-plasticity—plasticity and creep in elastic solids—a unified numerical solution approach. Int J Numer Methods Eng 8(4):821–845

17. Buffa G et al (2006) A continuum based fem model for friction stir welding—model development. Mater Sci Eng A 419(1):389–396

18. Ayer R et al (2005) Interface structure in a Fe–Ni friction stir welded joint. Scr Mater 53(12):1383–1387

19. Carslaw HS, Jaeger JC (1959) Conduction of heat in solids, 2nd edn. Clarendon Press, Oxford

20. Jain R, Pal SK, Singh SB (2016) A study on the variation of forces and temperature in a friction stir welding process: a finite element approach. J Manuf Process 23:278–286